High-Quality Graphene $p-n$ Junctions *via* Resist-free Fabrication and Solution-Based Noncovalent Functionalization

Hung-Chieh Cheng,[†,‡,§] Ren-Jye Shiue,[†,§] Chia-Chang Tsai,[†,‡] Wei-Hua Wang,[†,*] and Yit-Tsong Chen[†,‡,*]

[†]Institute of Atomic and Molecular Sciences, Academia Sinica, P.O. Box 23-166, Taipei 106, Taiwan, and [‡]Department of Chemistry, National Taiwan University, No. 1, Sec. 4, Roosevelt Road, Taipei 106, Taiwan. [§] These authors contributed equally to this work.

ABSTRACT An essential issue in graphene nanoelectronics is to engineer the carrier type and density and still preserve the unique band structure of graphene. We report the realization of high-quality graphene $p-n$ junctions by noncovalent chemical functionalization. A generic scheme for the graphene $p-n$ junction fabrication is established by combining the resist-free approach and spatially selective chemical modification process. The effectiveness of the chemical functionalization is systematically confirmed by surface topography and potential measurements, spatially resolved Raman spectroscopic imaging, and transport/magnetotransport measurements. The transport characteristics of graphene $p-n$ junctions are presented with observations of high carrier mobilities, Fermi energy difference, and distinct quantum Hall plateaus. The chemical functionalization of graphene $p-n$ junctions demonstrated in this study is believed to be a feasible scheme for modulating the doping level in graphene for future graphene-based nanoelectronics.

KEYWORDS: graphene · resist-free fabrication · surface potential · Raman imaging · $p-n$ junction · quantum Hall effect

Graphene, composed of a single layer of carbon atoms, is the thinnest material ever discovered and has been a focus of recent research. There is a vigorous trend to make graphene one of the basic materials for future electronics. Many graphene-based prototype devices have been demonstrated, including graphene nanoribbons,[1,2] quantum dots,[3] and $p-n$ junctions,[4] *etc*. One of the unique properties of graphene is its sensitivity to the environment due to the fact that the entire layer of carbon atoms has an immediate exposure to the surroundings. To date, several approaches have been applied to control the carrier type and modulate the carrier concentration in graphene by means of an electric field effect,[5] adsorptions of NO_2[6] and aromatic molecules,[7] and covalent functionalization.[8] In addition, graphene $p-n$ junction devices could be formed with a top-gated electric field,[4,9] chemical treatment by gas exposure,[10] polymer-induced doping,[11−13] electronic modification of the substrate,[14] and diazonium salts modification.[8,11,12]

Typically, the graphene $p-n$ junctions are fabricated by employing electron-beam lithography or photolithography processes. However, the resist residues from these processes are inevitable and can alter the electronic configurations and degrade carrier transport in graphene.[15] Moreover, these resist residues occupying the graphene surface could prevent further modification. To counter this problem, we developed a completely resist-free approach of preparing the graphene $p-n$ junctions. First, we fabricated the graphene devices using a shadow mask technique to avoid the residual resist polymer on the graphene surface; we also employed both vacuum and thermal annealing to further clean the graphene surface to achieve high carrier mobility. Second and more importantly, we developed a scheme of utilizing a microfluidic channel technique to realize spatially selective functionalization and solution-based chemical doping of graphene. These procedures have enabled us to achieve surface modification of graphene at a desired region without the resist residue problem.

To confirm the effectiveness of surface modification on graphene samples, we systematically performed surface topography and surface potential measurements by both atomic force microscopy (AFM) and Kelvin probe microscopy (KPM) in addition to spatially resolved Raman imaging with confocal micro-Raman spectrometry. We observed changes in both surface potential

* Address correspondence to wwang@gate.sinica.edu.tw, ytcchem@ntu.edu.tw.

Received for review November 26, 2010 and accepted February 1, 2011.

Published online February 15, 2011
10.1021/nn103221v

and Raman spectra upon functionalizing graphene with aromatic molecules. The results of surface potential measurements and Raman spectroscopic imaging clearly indicated spatially well-controlled surface modifications. Furthermore, by combining the noncovalent functionalization and the resist-free fabrication technique, we prepared graphene $p-n$ junctions and tested the electrical transport of the as-fabricated devices. The electrical measurements revealed evidence for high-quality graphene $p-n$ junctions, including high carrier mobility, the presence of Fermi energy difference, and Klein tunneling effect. Significantly, in quantum Hall (QH) regime, we observed a clear conductance plateau at 1 times the quantum of conductance, e^2/h, indicating a full-mixing of QH edge states at the interface of the graphene $p-n$ junction. Finally, the effects of the functionalization and fabrication processes on the transport properties are discussed.

The details of the experiment in this study are described in the Methods section. Briefly, single-layer graphene (SLG) was prepared by mechanical exfoliation from graphite flakes onto the SiO_2/Si substrates. The SLG was identified by optical microscopy and confirmed by Raman spectroscopy under ambient conditions. For the surface functionalization of SLG, a polydimethylsiloxane (PDMS) microfluidic channel ($6.25 \times 0.5 \times 0.05$ mm^3) was employed to implement the resist-free and selected-area surface modification. The following care was taken throughout the modification process: (i) The PDMS microchannel was aligned to a desired position on the SLG sheet with a spatial accuracy on the order of 1 μm; (ii) Any contamination or damage to the SLG sheet caused by contact to the PDMS microchannel was avoided; and (iii) following the surface modification, the PDMS microchannel was raised with great care to prevent lifting of the SLG sheet off the substrate. To fulfill these requirements, we developed a homemade $x-y-z$ manipulator system with a spatial resolution of $\sim$1 μm for aligning the PDMS microchannel. First, the $x-y-z$ manipulator was designed to couple an optical microscope to target a specific spot on SLG, as schematically illustrated in Figure 1. Before the alignment, the as-prepared PDMS microchannel was annealed at 110 °C for 30−45 min until an optimal working condition was reached; the annealing was done to avoid leaving any residual contamination of PDMS on the SLG sheet after removing the PDMS microchannel (Supporting Information section S1). The clean lift of the PDMS microchannel off SLG relies mainly on the extremely low surface energy[16] of the well-pretreated PDMS superficies.

To possess an *n*-type or *p*-type characteristic, the bipolar graphene could be modulated by doping a SLG with molecules containing either electron-donating or electron-withdrawing moieties. In this study, we chose 1,5-diaminonaphthalene (DAN) and 1-nitropyrene (NP)

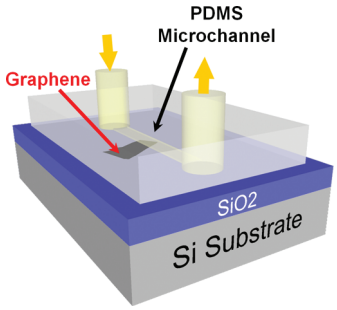

Figure 1. A schematic representation illustrating the selected-area surface modification. A graphene sheet is chemically modified with the assistance of a PDMS microfluidic channel through which solution-based chemical dopants can be delivered and deposited on the graphene surface.

as electron-donating[7,17] and electron-withdrawing molecules,[18,19] respectively, for surface potential mapping. Since DAN-modified samples exhibit less prominent *n*-type characteristics in electrical measurements with our method, NP and polyethylenimine (PEI) were chosen to demonstrate the *p*-type and *n*-type doping, respectively. The solution-based chemical modification of graphene was accomplished by pumping solutions containing dopants into the prealigned PDMS microchannel on the SLG sheet through a syringe pump at a rate of 0.3 mL/h for 1 h, as previously described (Figure 1). After the modification, the graphene devices were rinsed successively with ethanol and methanol for 45 min to remove excess dopant molecules.

RESULTS AND DISCUSSION

Figure 2 panels a and d display the optical images of two sets of SLG samples modified with DAN and NP, respectively, in which the doped regions are slightly darker than the pristine areas. In addition to the SLG sheet, there is a few layer graphene (FLG) sheet connected to the SLG in Figure 2a. The contrast between pristine and modified graphene becomes more obvious as higher density of molecules is applied (Supporting Information section S2). For comparison, we also conducted a control experiment of modifying the SLGs with the dopant molecules without aromatic rings; the result showed that the pristine and modified regions were indistinguishable by color contrast. This outcome indicates that the aromatic rings are responsible for the dopant molecules' association with graphene, probably through $\pi-\pi$ stacking, as discussed in the literature.[20]

The successful surface modification of SLGs could be verified by measuring their surface topography and surface potential by AFM and KPM, respectively. In particular, the KPM technique has been extensively used for probing the surface potential variation[21−23] as well as the local charge distribution. Some recent applications of this technique have demonstrated its potential as a tool for detecting the surface adsorbate,

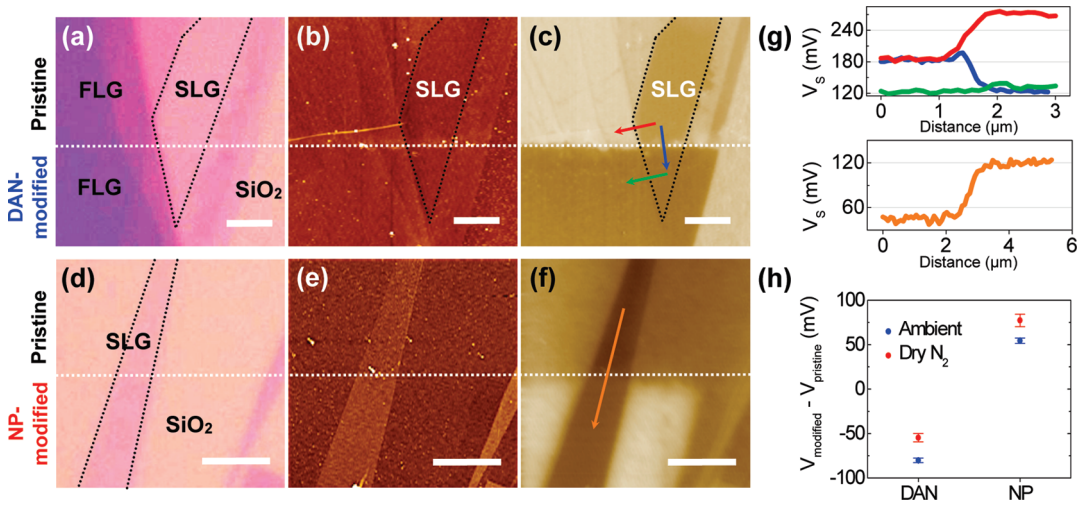

Figure 2. Microscopic imaging, surface topograph, and surface potential of partially modified graphenes. The optical microscopy (a, d), AFM (b, e), and KPM (c, f) images of pristine and surface-modified graphene sheets. The white scale bars in panels a−f are 3 μm. The central white dashed lines mark the boundaries between the pristine (upper sections) and modified (lower sections) regions of the graphene sheets. (a, d) Optical images of the SLG and FLG sheets modified with DAN and NP, respectively. The SLGs are enclosed by black dashed lines. The graphene samples in panels a and d were scanned by AFM and KPM, respectively, to produce the surface topographs (b, e) and the surface potential maps (c, f). The KPM images for the DAN-modified and NP-modified SLGs (the lower half of panels c and f, respectively) clearly show prominent rise and drop in potential (g) along the colored arrows across the pristine−modified boundary (blue and orange lines) and across the SLG−FLG boundary (red line). The green arrow (c) indicates the potential profile (green line, g) across the DAN-modified SLG−FLG boundary. (h) A plot showing the average differences in surface potential between pristine and DAN or NP-modified SLGs (*i.e.*, $V_{modified} - V_{pristine}$) measured under ambient air (blue dots) or dry N_2 (red dots).

such as water molecules,[24] and for determining the *n*- or *p*-type tendency of graphene after modification.[17,22] Shown in the lower sections of Figure 2 panels b and e are the AFM images of DAN-modified and NP-modified SLGs, respectively. It is noteworthy that the roughness of the modified region is close to that of pristine graphene, indicating a uniform modification of SLGs. In sharp contrast, the KPM images for DAN-modified (Figure 2c, lower section) and NP-modified (Figure 2f, lower section) SLGs clearly display considerable potential rise and fall (Figure 2g) along the colored arrows at the pristine−modified (blue and orange lines) and the SLG−FLG (red line) boundaries. Figure 2h summarizes the surface potential changes for DAN-modified and NP-modified SLGs; the KPM data were collected from three different sample sets at room temperature in both ambient (blue dots) and dry nitrogen (red dots) environments (Supporting Information section S3). The observed decrease (increase) in surface potential for DAN-modified (NP-modified) SLGs is in line with the corresponding *n*-type (*p*-type) doping characteristics, consistent with previous studies.[17] Although a distinct potential change occurs across the SLG−FLG boundary in the pristine region (red arrow, Figure 2c; red curve, Figure 2g), no significant potential difference exists across the SLG−FLG boundary in the DAN-modified region (green arrow, Figure 2c; green curve, Figure 2g). The similarity in surface potential between SLG and FLG in the DAN-modified area may be because KPM sensed only the charge characteristics of the DAN molecules associated with the topmost graphene sheet, neglecting the charge distributed in the sublayers of FLG. In view of the fact that the consistent surface-potential changes are created in both DAN-modified and NP-modified SLGs (Table S1 in Supporting Information section S3), we conclude that the surface functionalization assisted with the PDMS microchannel technique has proved to be a facile and effective method. This functionalization method also has the advantage of allowing the KPM measurements to use the same tip for simultaneously scanning the distinct domains to directly determine the surface-potential difference.

The surface-modified SLGs were also characterized by Raman spectroscopic imaging. An argon ion laser at 488 nm was used as an excitation source; the output power was limited to below 0.25 mW to avoid laser-induced heating or damage to the samples. Shown in Figure 3a is an optical image of a SLG partially modified with NP, in which the black dashed square specifies the area that was scanned for Raman imaging. A Raman mapping of the intensity ratio, *I*(2D)/*I*(G), that is, the 2D band intensity (at ~2700 cm^{-1}) divided by the G band intensity (at ~1590 cm^{-1}) is shown in Figure 3b. The mapping reveals a remarkable decrease from ~6 in the pristine region (the yellow-green section to the left) to ~2 in the NP-modified area (the blue section to the right), clearly indicating two distinct surfaces. Previous Raman studies of both electrochemically[25] doped and chemically[26] doped SLGs have also attributed the observed decrease in *I*(2D)/*I*(G) to a doping effect. For comparison, the Raman spectra for the two spots near

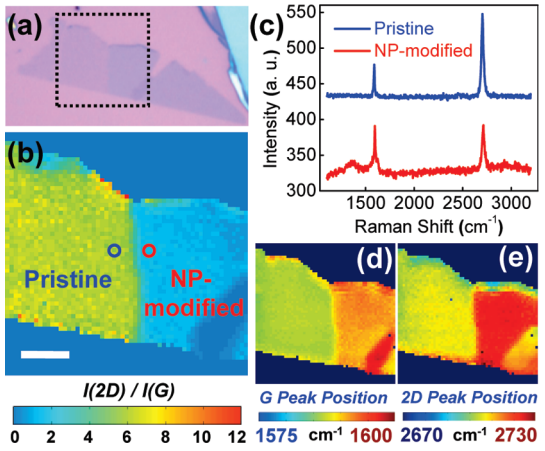

Figure 3. Raman imaging analysis of a partially modified graphene. (a) An optical micrograph of a SLG sheet partially modified with NP. (b) A spatially resolved Raman image of the partially NP-modified SLG obtained by Raman mapping over the area enclosed by the black dashed square in panel a. The spatially resolved Raman image represents the intensity ratio of *I*(2D)/*I*(G) on the 0−12 scale. The white scale bar is 3 μm. (c) Raman spectra for the two marked spots in panel b near the boundary between the pristine and NP-modified sections (the blue and red circles). (d, e) Raman mapping for the NP-modified SLG sheet in panel b: these images represent the G band absorption at 1575−1600 cm^{-1} (d) and the 2D band absorption at 2670−2730 cm^{-1} (e). These Raman mapping results reveal not only the homogeneity of the NP-modified area of SLG and its clear boundary with the pristine area, but also the Raman-shifts in the G band ($\Delta\nu \approx +8$ cm^{-1}) and 2D band ($\Delta\nu \approx +9$ cm^{-1}) of SLG due to NP-modification.

the boundary between the pristine region (blue circle in Figure 3b) and the NP-modified region (red circle) on the SLG are displayed in Figure 3c. While the Raman spectrum of pristine SLG (blue trace) exhibits the typical spectral characteristics of the G and 2D bands, the NP-modified SLG (red trace) shows not only a varied intensity ratio of *I*(2D)/*I*(G) but also additional peaks around 1200−1400 cm^{-1}, ascribable to the Raman signals for the NP molecules spectroscopically enhanced by underlying SLG.[27] As depicted in Figure 3d,e, the homogeneous modification of SLG with NP is also evidenced by the Raman-shift images, where the Raman-shifts caused by NP-modification at the G band ($\Delta\nu \approx +8$ cm^{-1}) and at the 2D band ($\Delta\nu \approx +9$ cm^{-1}) are clearly seen. The up-shifts of Raman signals due to the NP-modification have also been demonstrated to be characteristic of the *p*-type doping of SLG.[7,17,25] With this Raman imaging technique, we are able to visualize the chemically formed *p*−*n* junction and to verify the uniformity and the extent to which the SLG sheets were chemically modified.

Next, the electrical transport in the SLG devices is investigated. To prepare the SLG *p*−*n* junctions, pristine SLG sheets were first exfoliated onto a SiO_2/Si substrate which was precoated with hexamethyldisilazane (HMDS) to prevent ambient water from overlaying the ionized silanol groups on the SiO_2/Si substrate[28,29] (Supporting Information section S4). A commercial TEM grid was then used as a shield mask to define two contact pads. After the TEM grid was aligned to the SLG sheets, metal contacts of Ti/Au (5/55 nm) were deposited by e-beam evaporation in vacuum, with a base pressure of $\sim 2 \times 10^{-7}$ Torr. The as-fabricated SLG transistors were subsequently annealed at 350 °C for 6 h in an ultrahigh-vacuum chamber with a base pressure of $\sim 3 \times 10^{-9}$ Torr. The SLG transistors were then transferred into a He purged atmosphere of 20 Torr and were heated at 110 °C for 1.5 h to further remove water and/or oxygen adsorbed on the SLG devices during the transfer process. We performed 2-probe electrical measurements on the SLG transistors using a standard lock-in technique with a current bias of $I_{AC} = 100$ nA$_{rms}$. Differential resistance is defined as $R = dV_{sd}/dI$, where V_{sd} is the source−drain voltage. The quantum Hall effect (QHE) was measured at $T = 1.9$ K with a maximum magnetic field of $\mathbf{B} = 9$ T perpendicular to the SLG sheets. It is noted that, in the two-terminal geometry, the measured resistance includes the graphene resistance and the contact resistance, while its effects are discussed in Supporting Information section S5.

Figure 4a shows the resistivity ρ as a function of V_G for a SLG device before (black) and after (red) modification with NP. The charge neutrality point (CNP) is observed to move from −3 to 11 V, which is, again, characteristic of the *p*-type doping caused by NP molecules and is consistent with the surface-potential measurements by KPM and the Raman spectroscopic results discussed above. The induced carrier density, deduced from the voltage difference at the CNP, can be estimated to be 1×10^{12} cm^{-2}. The mobility of the charge carriers in pristine SLG before functionalization is 15 000 cm^2/(V s) for holes and 15 200 cm^2/(V s) for electrons. The high carrier mobilities in the SLG device convincingly demonstrate a well-controlled surface condition as a consequence of both substrate treatment and postfabrication annealing (Supporting Information section S4). This clean graphene surface is absolutely crucial for the subsequent modification and the resulting doping effects. After functionalization, the NP-modified SLG device exhibits the carrier mobility of 8900 cm^2/(V s) for holes and 4400 cm^2/(V s) for electrons. The doping molecules inevitably introduce an extra source of carrier scattering and degrade the carrier mobility; however, the mobility remains sufficiently high, as evidenced by the observation of distinct QHE that is discussed in the following section. To explore the bipolar characteristics of graphene, another SLG device was modified with *n*-type dopant PEI. The *n*-type dopant DAN was not used because the CNP shift was found to be very small by flowing solutions containing DAN through a microfluidic channel. The measured $\rho - V_G$ curves for the PEI-doped device are shown in Figure 4b. The CNP of the PEI-doped SLG is seen to move from 0 to −3 V, a trend opposite to what

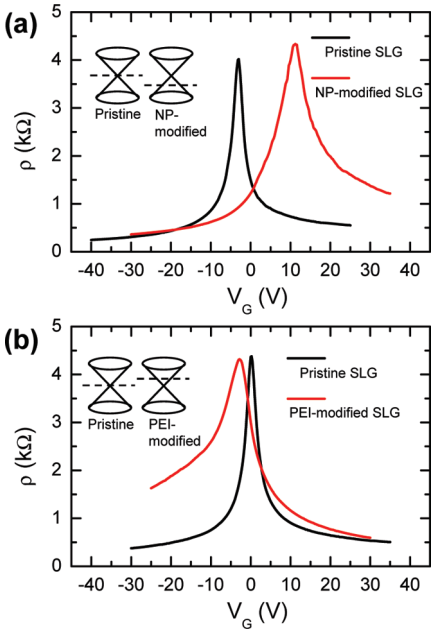

Figure 4. Electrical properties of chemical modified graphene devices. The $\rho-V_G$ curves of a SLG device before (black) and after (red) being modified with NP (a) and with PEI (b). For the NP-modified device, the CNP shifts from −3 to 11 V, indicating a *p*-type doping. The field-effect mobility for holes (electrons) is 15000 cm^2/(V s) (15200 cm^2/(V s)) before the NP-modification and is 8900 cm^2/(V s) (4400 cm^2/(V s)) after the NP-modification. The CNP of the PEI-modified SLG device shifts from 0 to −3 V in the opposite direction to what is observed in the NP-modified device, indicating an *n*-type doping. The hole (electron) mobility is 12 300 cm^2/(V s) (11 400 cm^2/(V s)) before the PEI-modification, and it is 2400 cm^2/(V s) (5400 cm^2/(V s)) after the PEI-modification. The insets schematically show the Fermi level shift caused by NP (*p*-type) or PEI (*n*-type) doping.

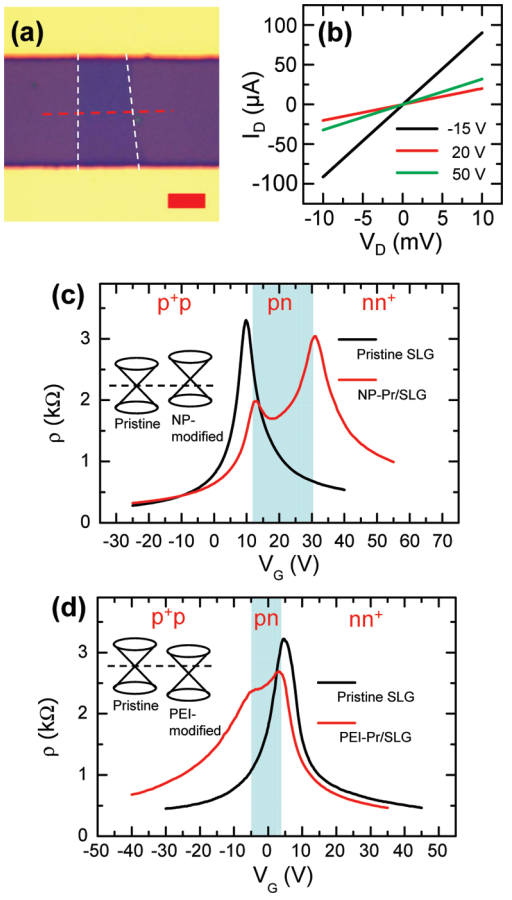

Figure 5. Electrical transport measurements of resist-free graphene *p*−*n* junction devices. (a) A typical optical micrograph of the NP-Pr/SLG device. The white dashed lines mark the edges of a SLG sheet and the red dashed line indicates the boundary of the NP-modified (upper) and pristine (lower) regions. (b) The I_D-V_D characteristic of the NP-Pr/SLG device at different gate voltages. The curves for $V_G = -15$ V (black), 20 V (red), and 50 V (green) correspond to the p^+-p, $p-n$, and $n-n^+$ transport, respectively. (c) The $\rho-V_G$ curves of the NP-Pr/SLG device before (black) and after (red) functionalization. The red curve exhibits resistivity maxima at 10 and 30 V; meanwhile, three distinct carrier transport regions, namely p^+-p, $p-n$, and $n-n^+$, can be identified. The inset schematically shows the Fermi energy difference between the two regions in the NP-Pr/SLG device. (d) The $\rho-V_G$ curves of the PEI-Pr/SLG device before (black) and after (red) functionalization. The two CNPs found at +4 and −5 V divide the carrier transport into three categories similar to the case of the NP-Pr/SLG device. The inset schematically shows the Fermi energy difference in the PEI-Pr/SLG device.

is observed in the NP-modified sample, demonstrating an *n*-type doping by PEI. The carrier mobility before (after) the PEI modification was 12 300 (2400) cm^2/(V s) for holes and 11 400 (5400) cm^2/(V s) for electrons.

To further investigate the electrical transport of a SLG *p*−*n* junction, we prepared a device with the SLG channel doped only halfway with NP. Hereafter, this SLG *p*−*n* junction device with a half NP-doped and half undoped (pristine) channel will be referred to as NP-Pr/SLG. A typical optical image of this NP-Pr/SLG device is shown in Figure 5a, where the white dashed lines mark the edges of a SLG sheet, and the red dashed line marks the clear boundary between the NP-doped region (upper side) and pristine region (lower side). A measured resistivity ρ as a function of V_G for this NP-Pr/SLG device is presented in Figure 5c (red curve) and is compared with that of the pristine state (black curve). The pristine SLG device presented here exhibits a single CNP at $V_G \approx 10$ V, and its field-effect mobility is 10 000 and 7000 cm^2/(V s) for holes and electrons, respectively. For the NP-Pr/SLG device, we observe an extra peak at $V_G \approx 30$ V after forming the *p*−*n* junction, while the other peak remains close to $V_G \approx 10$ V. We note that the proximity of the CNP in the pristine SLG region signifies that little alteration occurs to the Fermi level of SLG when employing our solution-based microchannel functionalization technique. Because NP is a *p*-type dopant for graphene, it lowers the Fermi level of graphene in the doped region (see Figure 5c inset). The shift in Fermi level creates a junction across the boundary and causes the Fermi energy difference between the two regions as a result of equilibrium of the Fermi level. This energy difference of the Dirac points revealed by the double CNP peaks clearly confirms the existence of the SLG *p*−*n* junction. The energy difference of the two CNPs in different regions

can be estimated by the relation[5,30] $\Delta E = \hbar v_F(\pi\alpha|V_{CNP,pristine} - V_{CNP,doped}|)^{1/2}$, where $\alpha \approx 7.0 \times 10^{10}$ cm^{-2} V^{-1} is the gate voltage to carrier density conversion factor (Supporting Information section S6). For the NP-Pr/SLG $p-n$ junction, the value of $|V_{CNP,pristine} - V_{CNP,doped}|$ is ~20 V and the energy separation is $\Delta E \approx 140$ meV. Furthermore, on the basis of the two separated CNPs, three distinct regions in the $\rho-V_G$ graph of the SLG $p-n$ junction can be identified as p^+-p, $p-n$, and $n-n^+$ regimes.

The tunneling effect across a SLG $p-n$ junction is intriguing because of the unique band structure of graphene. For conventional semiconductor $p-n$ junctions, it is well-known that the I_D-V_D curves exhibit a rectifying behavior. However, due to the chirality of the massless Dirac fermions of graphene, the back scattering by a potential barrier is suppressed for the carriers in graphene (Klein tunneling[31,32]). Here, we demonstrate this peculiar behavior by measuring the I_D-V_D curves for the three different regimes (p^+-p, $p-n$, and $n-n^+$) of the NP-Pr/SLG device. In Figure 5b, the observed linearity of the I_D-V_D curves, despite the energy barrier at the boundary, is consistent with Klein tunneling effect.

For a comparative study, another SLG $p-n$ junction was fabricated by doping the SLG channel halfway with PEI (referred to as PEI-Pr/SLG), similar to the aforementioned NP-Pr/SLG device with the *p*-type NP replaced with the *n*-type PEI. Both a CNP peak splitting and the Fermi energy difference ($\Delta E \approx 100$ meV) are observed for the PEI-Pr/SLG device. For the PEI-Pr/SLG device, however, the additional peak of CNP occurs at lower energy relative to that of pristine SLG, as indicated in Figure 5d. This extra peak of CNP stems from the fact that PEI is an *n*-type dopant to graphene[11] and, therefore, raises the Fermi level in the doped region (see Figure 5d inset.)

To reach the QH regime, the SLG devices are cooled to low temperature and subjected to a magnetic field perpendicular to the SLG sheets; in the QH regime, the electrical conductance evolves into a characteristic series of QH plateau. In these QH plateau regions, the electrical conductance remains constant while the carrier density varies as a function of V_G. Moreover, the conductance plateaus occur at well-known half-integers, as a consequence of the Dirac-like energy spectrum of SLG.[30,33] For each quantum state, there are $|\nu|$ edge states to propagate, where ν is a filling factor that corresponds to the quantized values of $\nu = \pm 2, \pm 6, \pm 10, ...$[34]

In our QHE investigation, we performed two terminal conductance measurements on the SLG device as a function of V_G at $T = 1.9$ K and **B** = 9 T. It is seen in Figure 6a that the conductance plateaus developed with the quantized values of 2 e^2/h and 6 e^2/h for both electrons and holes, as expected from the half-integer QHE occurring in SLG with the filling factors of $\nu = \pm 2, \pm 6$. These QH plateaus that appear at the predicted filling factors unambiguously confirm that the graphene sheet under study is single layer with high mobility carriers. The conductance peaks aligned with plateau centers are attributed to the presence of nonzero longitudinal conductance. In fact, the distortion features between plateaus reflect the aspect ratio of the device, W/L, where W is the width of the device and L is the length between contact electrodes[35,36] (Supporting Information section S7).

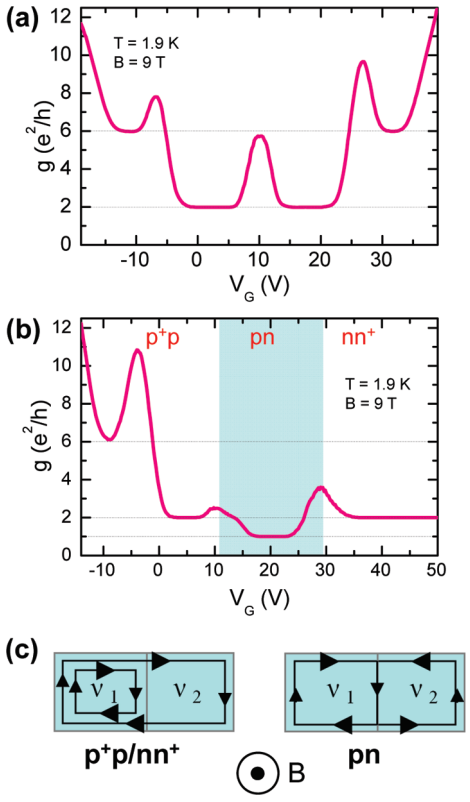

Figure 6. Quantum Hall effect in resist-free graphene $p-n$ junction devices. (a) QHE of a SLG device. The transport characteristics are measured at the temperature of $T = 1.9$ K and under the magnetic field of B = 9 T, applied perpendicular to the graphene sheet. The conductance plateaus at 2 e^2/h and 6 e^2/h correspond to the filling factors of $\nu = \pm 2, \pm 6$ for electrons and holes and are in accordance with the expected half-integer QHE in SLG. (b) QHE of the NP-Pr/SLG device at $T = 1.9$ K and B = 9 T perpendicular to the graphene plane. This NP-Pr/SLG $p-n$ junction was made by taking the same device presented in panel a for NP-modification. In the p^+-p and $n-n^+$ regions, QH plateaus with the filling factors of $\nu = \pm 2, -6$ can be observed. In the $p-n$ junction regime, however, a new QH plateau at $1e^2/h$ can be identified, indicating a full mixing of $\nu_1 = +2$ and $\nu_2 = -2$ edge states. (c) Edge state circulation of the graphene $p-n$ junctions in QH regime. (Left panel) In the unipolar regime, both edge states circulate in the same direction and only the edge states with fewer modes could encircle the entire $p-n$ junction. (Right panel) On the contrary, edge currents in *p*- and *n*- regions circulate in opposite directions and mix at the $p-n$ interface in the bipolar regime.

We now focus on the transport characteristics of the noncovalently functionalized SLG $p-n$ junction that exhibits a clear QHE despite the additional scattering introduced by the dopant molecules. Depending on

the combination of carrier types, the SLG $p-n$ junction can be categorized into a unipolar regime (p^+-p or $n-n^+$) and a bipolar regime ($p-n$). In the unipolar regime, the edge currents in both domains circulate in the same direction and only the edge current with a relatively small number of modes can encircle the entire $p-n$ junction (left schematic in Figure 6c). Therefore, the conductance of the $p-n$ junction in the unipolar regime can be expressed as[4,37]

$$g_{nn} = g_{pp} = \min(|\nu_1|, |\nu_2|) \times e^2/h \quad (1)$$

In Figure 6b, we show the QH features of the NP-Pr/SLG $p-n$ junction as a function of V_G at $T = 1.9$ K and $\mathbf{B} = 9$ T. This NP-Pr/SLG $p-n$ junction was made by performing a NP-modification on the device whose QHE is shown in Figure 6a. For $V_G < 10$ V and $V_G > 30$ V, it is apparent that the conductance plateaus at $2e^2/h$ are observable for both carrier types and a partially developed plateau of higher order ($6e^2/h$) is observable for holes. It is noteworthy that the observed accuracy of the quantized conductance demonstrates that the modification does not significantly alter the Dirac spectrum while effectively doping the SLG $p-n$ junction.

An electron–hole asymmetry in the unipolar regions can be observed as the width of the $2e^2/h$ plateau in the $n-n^+$ region is larger than that in the p^+-p region. The larger $2e^2/h$ plateau in the $n-n^+$ region may be attributed to the asymmetry in V_G dependence of Landau level that originated from the NP modification. The center of the conductance plateaus are aligned with the filling factors $\nu = nh/e\mathbf{B} = (h/e\mathbf{B})\alpha V_G$. For the pristine region of the graphene $p-n$ junction, the gate voltage to density conversion factor, α, simply corresponds to the capacitance of the gate oxide. On the other hand, a smaller α in the $n-n^+$ region is expected for the NP-modified region since NP is an electron-withdrawing molecule and the same V_G induces smaller electron density. Moreover, in the p^+-p region, the edge currents that encircle the entire $p-n$ junction are determined by the pristine region which exhibits a smaller number of mode (lower hole density). On the contrary, in the $n-n^+$ region, the edge currents are determined by the NP-modified region (lower electron density). Therefore, the effective smaller α in the NP-modified region makes the center of the plateau appear at higher V_G in the $n-n^+$ region. Moreover, a wider plateau in the $n-n^+$ region would occur based on the same density range because of the effective smaller α in the NP-modified region.

In contrast with the unipolar regime, a distinct conductance plateau was observed at a nonconventional quantization value of $1e^2/h$ in the bipolar regime over the range of $15 < V_G < 25$ V, as seen in Figure 6b. This new plateau can be understood by considering the mode mixing at the interface of the NP-Pr/SLG $p-n$ junction. In the QH regime, the bulk of both p and n regions becomes insulating due to Anderson localization in the presence of impurities. The carrier transport then relies on chiral edge states which circulate at opposite directions in the bipolar regime. At the $p-n$ interface where two edge states meet (right schematic in Figure 6c), a mode mixing could occur provided that the following two conditions are met. First, the electrochemical potentials of the two edge states have to be at full equilibrium at the joining point. Second, a compressible channel at the $p-n$ interface has to exist so that the merged QH mode can flow within the channel. If the edge currents from the two domains can fully mix, the QH plateaus in the two-terminal conductance should occur at the following quantized values:[4,36]

$$g_{pn} = \frac{|\nu_1||\nu_2|}{|\nu_1| + |\nu_2|} \times e^2/h = 1, \frac{3}{2}, 3, \frac{5}{3}, \ldots \times e^2/h \quad (2)$$

Accordingly, the NP-Pr/SLG $p-n$ junction in the bipolar regime exhibits a QH plateau at $1e^2/h$, corresponding to the mixed state of $\nu_1 = +2$ and $\nu_2 = -2$. In view of the conductance plateau lying at $1e^2/h$, a full mixing of the two edge states at the $p-n$ interface is evident. Although we have employed a novel fabrication protocol for graphene $p-n$ junctions, the QHE exhibits the same quantized conductance as top electrical gating devices.[4] This repeatedly confirms the universality of the QHE in spite of the detail of the system, such as composing materials or dimensions of the channels.

In summary, we have successfully demonstrated the effectiveness of noncovalent functionalization of graphene by fabricating the SLG $p-n$ junctions using a completely resist-free approach and spatially selective chemical modification process. The chemically modified SLG samples were systematically characterized by optical microscopy, surface topography and potential measurements, and spatially resolved Raman spectroscopic imaging. The high quality of the SLG $p-n$ junctions is supported by the observations of the high carrier mobilities, the Fermi energy difference, and the noticeable nonconventional QHE.

METHODS

SiO_2/Si Substrates Pretreated with HMDS Prior to SLG Device Fabrication. In preparing SLG sheets by mechanical exfoliation from graphite flakes onto a SiO_2/Si substrate, the ionized silanol groups on the SiO_2 layer and other substrate defects could spoil the electronic transport of the as-prepared SLG devices. These ionized silanol groups that tend to be the adsorption sites of dipolar molecules (*e.g.*, water), however, could be reduced *via* a reaction with hexamethyldisilazane (HMDS) (Aldrich, reagent grade, ≥99%). The resultant hydrophobic methylsilyl surface on the

SiO_2 layer could prevent the deposited SLG sheets from being interfered by moisture contamination and substrate defects.

In the SLG preparation, the SiO_2/Si substrate was sonicated first in acetone and then in isopropyl alcohol and was subsequently cleaned in oxygen plasma at 100 W for 5 min to remove organic contaminants. Before the SiO_2/Si substrate was suspended in a two-neck flask for surface functionalization, the flask was preheated to 110 °C for 10 min to remove the surface-adsorbed water and then evacuated for 10 min prior to the addition of 0.5 mL HMDS. The flask was subsequently kept at 80 °C for ~20 h to ensure a sufficient reaction of the HMDS vapor with the silanol groups on the SiO_2 surface. After the reaction, the SiO_2/Si substrate was again sonicated briefly in acetone and isopropyl alcohol to remove excess HMDS and was blow-dried with N_2. The pretreated SiO_2/Si substrate was then ready for the SLG exfoliation.

Solution-Based Chemical Modification for the Formation of SLG *p*−*n* Junctions. We chose 1,5-diaminonaphthalene (abbreviated as DAN, Aldrich, 97%) and 1-nitropyrene (abbreviated as NP, Sigma, 99%) as *n*-type and *p*-type dopant molecules, respectively, to be used to modify the SLG sheets. In forming the SLG *p*−*n* junctions, the PDMS microchannel was aligned to cover the SLG channel halfway using a homemade *x*−*y*−*z* manipulator with a spatial resolution of 1 μm. After the PDMS microfluidic channel was coupled to the SLG sheet at a desired position, either 20 mM DAN in ethanol or 5 mM NP in methanol was pumped into the PDMS microchannel and was delivered onto the SLG surface through a syringe pump (KD Scientific, KD-101) at 0.3 mL/h for 1 h. After the surface modification, the SLG was rinsed by flushing methanol and ethanol into the PDMS microchannel at a flow rate of 0.5 mL/h for 45 min to remove excess dopant molecules from the SLG surface.

In the surface modification of SLG, we also used polyethylenimine (abbreviated as PEI, Fluka, 50% (w/v) in H_2O) as another *n*-type dopant. The PEI solution from the commercial source was further diluted in ethanol to 1:1 (v/v) and the mixture was then pumped into the PDMS microchannel to reach the SLG surface. During the modification, the PEI solution was kept without flow inside the PDMS microchannel to react with the SLG surface for 1 h. After the modification, the functionalized SLG surface was again rinsed by flushing ethanol into the PDMS microchannel at a flow rate of 0.5 mL/h for 45 min.

Raman Spectroscopic Imaging to Characterize the Spatially Selective Modification. The micro-Raman spectroscopic imaging technique was employed to characterize the SLG *p*−*n* junctions using a commercial Raman spectrometer (NTEGRA, NT-MDT). An argon ion laser at $\lambda = 488$ nm was used as an excitation source for the Raman imaging. The laser beam was focused by a 100× objective onto the SLG sample, keeping the output power below 0.25 mW to avoid laser-induced heating or damage to the SLG sheets. The Raman scattering signals were finally collected by a CCD camera (Andor Technology, DV401) that was integrated into the NTEGRA spectral system. The Raman mapping data were obtained by scanning the sample over the 15.25 × 15.25 μm^2 area (the number of points was preset to 60 × 60) with a step size of ~0.258 μm and with the exposure time at each point of 3.5 s. The Raman spectrum was recorded for each point over the range of 420−3300 cm^{-1}; the frequency was calibrated to the major peak of a Si wafer at 520.7 cm^{-1}.

Fabrication of SLG Field-Effect Devices. Degenerate *p*-type SiO_2/Si substrates ($\rho = 0.01$ Ω-cm) with a 300-nm-thick thermally grown oxide were treated with HMDS (as discussed in the first section of Methods) prior to the fabrication of SLG field-effect devices. After SLG sheets were exfoliated onto the substrate, we identified the as-prepared SLG sheets under an optical microscope by comparing its contrast with the substrate. The Raman spectra of graphene sheets were also taken using the NTEGRA spectral system to further confirm the layer numbers. To define the electrode pattern of the SLG device, a commercial transmission electron microscopy (TEM) grid (Electron Microscopy Sciences, 200 mesh) was used as a shadow mask. A proper alignment of the TEM grid to a desired position on the SLG sheet was accomplished by coupling an optical microscope to the aligner mounted on the *x*−*y*−*z* manipulator. After the alignment, Ti/Au (5/55 nm) was deposited on the SLG sheet with an e-beam evaporator (Temescal) in a high-vacuum chamber with a base pressure of ~2×10^{-7} Torr. After the metal deposition, the SLG devices were heated to 350 °C for 6 h in another ultrahigh-vacuum chamber with a base pressure of ~3×10^{-9} Torr and were subsequently transferred to the He refrigerator (Quantum Design PPMS) with a He purged atmosphere of 20 Torr. The SLG devices were thermally annealed again at 110 °C for 1.5 h and cooled down to 10 K before electrical measurements.

Electrical Measurements. The electrical measurements were performed using a standard lock-in technique with a current bias of $I_{AC} = 100$ nA_{rms} and a modulation frequency of 147 Hz. Differential resistance is defined as $R = dV_{sd}/dI$, where V_{sd} is the source−drain voltage. The voltage signal was amplified with a voltage preamplifier (Stanford Research Systems, SR560) and then sent to a lock-in amplifier (Stanford Research Systems, SR830). The gate voltage was applied by a DC source (Keithley 2400). In the QH regime, the measurement was performed at $T =$ 1.9 K. We applied the magnetic field perpendicular to the SLG surface using a commercial measurement system (Quantum Design PPMS) in the range of $\mathbf{B} = -9$ to 9 T while recording the $\rho - V_G$ data at either $I_{AC} = 100$ nA_{rms} or 10 nA_{rms}. The $I_D - V_D$ curves displayed in Figure 5b were measured by recording the source−drain current with a DC multimeter (Keithley 2400) while scanning the DC voltage bias.

Acknowledgment. This work was supported by the National Science Council of Taiwan under contract numbers NSC 98-2112-M-001-005-MY3 and NSC 99-2627-M-002-001.

Supporting Information Available: Reduction of residual PDMS contamination, optical microscopy color contrast analysis, details in KPM measurement, device performance comparison between HMDS-modified and SiO_2/Si substrates, contact resistance in two-terminal configuration, estimate of the gate voltage to carrier density conversion factor, and two-terminal conductance measurement in QH regime. This material is available free of charge *via* the Internet at http://pubs.acs.org.

REFERENCES AND NOTES

1. Li, X.; Wang, X.; Zhang, L.; Lee, S.; Dai, H. Chemically Derived, Ultrasmooth Graphene Nanoribbon Semiconductors. *Science* **2008,** *319*, 1229–1232.
2. Han, M. Y.; Ouml; zyilmaz, B.; Zhang, Y.; Kim, P. Energy Band-Gap Engineering of Graphene Nanoribbons. *Phys. Rev. Lett.* **2007,** *98*, 206805.
3. Ponomarenko, L. A.; Schedin, F.; Katsnelson, M. I.; Yang, R.; Hill, E. W.; Novoselov, K. S.; Geim, A. K. Chaotic Dirac Billiard in Graphene Quantum Dots. *Science* **2008,** *320*, 356–358.
4. Williams, J. R.; DiCarlo, L.; Marcus, C. M. Quantum Hall Effect in a Gate-Controlled *p*−*n* Junction of Graphene. *Science* **2007,** *317*, 638–641.
5. Novoselov, K. S.; Geim, A. K.; Morozov, S. V.; Jiang, D.; Zhang, Y.; Dubonos, S. V.; Grigorieva, I. V.; Firsov, A. A. Electric Field Effect in Atomically Thin Carbon Films. *Science* **2004,** *306*, 666–669.
6. Schedin, F.; Geim, A. K.; Morozov, S. V.; Hill, E. W.; Blake, P.; Katsnelson, M. I.; Novoselov, K. S. Detection of Individual Gas Molecules Adsorbed on Graphene. *Nat. Mater.* **2007,** *6*, 652–655.
7. Dong, X.; Fu, D.; Fang, W.; Shi, Y.; Chen, P.; Li, L. J. Doping Single-Layer Graphene with Aromatic Molecules. *Small* **2009,** *5*, 1422–1426.
8. Koehler, F.; Luechinger, N.; Ziegler, D.; Athanassiou, E.; Grass, R.; Rossi, A.; Hierold, C.; Stemmer, A.; Stark, W. Permanent Pattern-Resolved Adjustment of the Surface Potential of Graphene-like Carbon through Chemical Functionalization. *Angew. Chem., Int. Ed.* **2009,** *48*, 224–227.
9. Ki, D. K.; Nam, S. G.; Lee, H. J.; Ozyilmaz, B. Dependence of Quantum-Hall Conductance on the Edge-State Equilibration Position in a Bipolar Graphene Sheet. *Phys. Rev. B* **2010,** *81*, 033301.
10. Lohmann, T.; von Klitzing, K.; Smet, J. H. Four-Terminal Magneto-Transport in Graphene *p*−*n* Junctions Created by Spatially Selective Doping. *Nano Lett.* **2009,** *9*, 1973–1979.

11. Farmer, D. B.; Golizadeh-Mojarad, R.; Perebeinos, V.; Lin, Y.-M.; Tulevski, G. S.; Tsang, J. C.; Avouris, P. Chemical Doping and Electron-Hole Conduction Asymmetry in Graphene Devices. *Nano Lett.* **2008,** *9*, 388–392.
12. Farmer, D. B.; Lin, Y.-M.; Afzali-Ardakani, A.; Avouris, P. Behavior of a Chemically Doped Graphene Junction. *Appl. Phys. Lett.* **2009,** *94*, 213106–3.
13. Brenner, K.; Murali, R. Single Step, Complementary Doping of Graphene. *Appl. Phys. Lett.* **2010,** *96*, 063104–3.
14. Chiu, H.-Y.; Perebeinos, V.; Lin, Y.-M.; Avouris, P. Controllable $p-n$ Junction Formation in Monolayer Graphene Using Electrostatic Substrate Engineering. *Nano Lett.* **2010,** *10*, 4634–4639.
15. Ishigami, M.; Chen, J. H.; Cullen, W. G.; Fuhrer, M. S.; Williams, E. D. Atomic Structure of Graphene on SiO_2. *Nano Lett.* **2007,** *7*, 1643–1648.
16. Allen, M. J.; Tung, V. C.; Gomez, L.; Xu, Z.; Chen, L. M.; Nelson, K. S.; Zhou, C.; Kaner, R. B.; Yang, Y. Soft Transfer Printing of Chemically Converted Graphene. *Adv. Mater.* **2009,** *21*, 2098–2102.
17. Dong, X.; Shi, Y.; Chen, P.; Ling, Q.; Huang, W. Aromatic Molecules Doping in Single-Layer Graphene Probed by Raman Spectroscopy and Electrostatic Force Microscopy. *Jpn. J. Appl. Phys.* **2010,** *49*, 01AH04.
18. Star, A.; Han, T.-R.; Gabriel, J.-C. P.; Bradley, K.; Grüner, G. Interaction of Aromatic Compounds with Carbon Nanotubes: Correlation to the Hammett Parameter of the Substituent and Measured Carbon Nanotube FET Response. *Nano Lett.* **2003,** *3*, 1421–1423.
19. Carrasco, E. A.; Campos-Vallette, M.; Leyton, P.; Diaz, G.; Clavijo, R. E.; García-Ramos, J. V.; Inostroza, N.; Domingo, C.; Sanchez-Cortes, S.; Koch, R. Study of the Interaction of Pollutant Nitro Polycyclic Aromatic Hydrocarbons with Different Metallic Surfaces by Surface-Enhanced Vibrational Spectroscopy (SERS and SEIR). *J. Phys. Chem. A* **2003,** *107*, 9611–9619.
20. Hunter, C. A.; Sanders, J. K. M. The Nature of $\pi-\pi$ Interactions. *J. Am. Chem. Soc.* **1990,** *112*, 5525–5534.
21. Datta, S. S.; Strachan, D. R.; Mele, E. J.; Johnson, A. T. C. Surface Potentials and Layer Charge Distributions in Few-Layer Graphene Films. *Nano Lett.* **2008,** *9*, 7–11.
22. Shi, Y.; Kim, K. K.; Reina, A.; Hofmann, M.; Li, L.-J.; Kong, J. Work Function Engineering of Graphene Electrode *via* Chemical Doping. *ACS Nano* **2010,** *4*, 2689–2694.
23. Yu, Y.-J.; Zhao, Y.; Ryu, S.; Brus, L. E.; Kim, K. S.; Kim, P. Tuning the Graphene Work Function by Electric Field Effect. *Nano Lett.* **2009,** *9*, 3430–3434.
24. Moser, J.; Verdaguer, A.; Jimenez, D.; Barreiro, A.; Bachtold, A. The Environment of Graphene Probed by Electrostatic Force Microscopy. *Appl. Phys. Lett.* **2008,** *92*, 123507–3.
25. Das, A; Pisana, S; Chakraborty, B; Piscanec, S; Saha, S. K.; Waghmare, U. V.; Novoselov, K. S.; Krishnamurthy, H. R.; Geim, A. K.; Ferrari, A. C.; Sood, A. K. Monitoring Dopants by Raman Scattering in an Electrochemically Top-Gated Graphene Transistor. *Nat. Nanotechnol.* **2008,** *3*, 210–215.
26. Voggu, R.; Das, B.; Rout, C. S.; Rao, C. N. R. Effects of Charge Transfer Interaction of Graphene with Electron Donor and Acceptor Molecules Examined Using Raman Spectroscopy and Cognate Techniques. *J. Phys.: Condens. Matter* **2008,** *20*, 472204.
27. Ling, X.; Xie, L.; Fang, Y.; Xu, H.; Zhang, H.; Kong, J.; Dresselhaus, M. S.; Zhang, J.; Liu, Z. Can Graphene Be Used as a Substrate for Raman Enhancement?. *Nano Lett.* **2009,** *10*, 553–561.
28. Lafkioti, M.; Krauss, B.; Lohmann, T.; Zschieschang, U.; Klauk, H.; Klitzing, K. v.; Smet, J. H. Graphene on a Hydrophobic Substrate: Doping Reduction and Hysteresis Suppression under Ambient Conditions. *Nano Lett.* **2010,** *10*, 1149–1153.
29. Kim, W.; Javey, A.; Vermesh, O.; Wang, Q.; Li, Y.; Dai, H. Hysteresis Caused by Water Molecules in Carbon Nanotube Field-Effect Transistors. *Nano Lett.* **2003,** *3*, 193–198.
30. Novoselov, K. S.; Geim, A. K.; Morozov, S. V.; Jiang, D.; Katsnelson, M. I.; Grigorieva, I. V.; Dubonos, S. V.; Firsov, A. A. Two-Dimensional Gas of Massless Dirac Fermions in Graphene. *Nature* **2005,** *438*, 197–200.
31. Katsnelson, M. I.; Novoselov, K. S.; Geim, A. K. Chiral Tunnelling and the Klein Paradox in Graphene. *Nature Phys.* **2006,** *2*, 620–625.
32. Stander, N.; Huard, B.; Goldhaber-Gordon, D. Evidence for Klein Tunneling in Graphene $p-n$ Junctions. *Phys. Rev. Lett.* **2009,** *102*, 026807.
33. Zhang, Y.; Tan, Y.-W.; Stormer, H. L.; Kim, P. Experimental Observation of the Quantum Hall Effect and Berry's Phase in Graphene. *Nature* **2005,** *438*, 201–204.
34. Gusynin, V. P.; Sharapov, S. G. Unconventional Integer Quantum Hall Effect in Graphene. *Phys. Rev. Lett.* **2005,** *95*, 146801.
35. Abanin, D. A.; Levitov, L. S. Conformal Invariance and Shape-Dependent Conductance of Graphene Samples. *Phys. Rev. B* **2008,** *78*, 035416.
36. Williams, J. R.; Abanin, D. A.; DiCarlo, L.; Levitov, L. S.; Marcus, C. M. Quantum Hall Conductance of Two-Terminal Graphene Devices. *Phys. Rev. B* **2009,** *80*, 045408.
37. Abanin, D. A.; Levitov, L. S. Quantized Transport in Graphene $p-n$ Junctions in a Magnetic Field. *Science* **2007,** *317*, 641–643.